Materials Horizons

ROYAL SOCIETY OF CHEMISTRY

COMMUNICATION

View Article Online
View Journal

Check for updates

Cite this: DOI: 10.1039/d6mh00418k

Received 5th March 2026,
Accepted 15th May 2026

DOI: 10.1039/d6mh00418k

rsc.li/materials-horizons

Flexoelectric polarization–electric field coupling-driven phase transformation in epitaxial films

Seong Min Park,[a] WooJun Seol,[a] Su Yong Lee,[b] Hyunjin Joh,[a] Keeyong Lee,[c] Sang Ho Oh,[c] Hyeon Jun Lee*[d] and Ji Young Jo *[ae]

Nanoscale phase transformations at interfaces enable unprecedented control over the structure and functionalities of low-dimensional materials. Flexoelectric polarization, universally produced by the strain gradient in all dielectrics, can be directly coupled to an external electric field and amplified at nanoscale interfaces. Here, we show that this coupling leads to an electromechanical response and a reversible phase transformation at a nanoscale flexoelectric layer between morphotropic phases. In epitaxial $BiFeO_3$–$BaTiO_3$ thin films, the external electric field triggers a transient structural transition from an interfacial flexoelectric layer to crystalline phases, as revealed by *in situ* time-resolved X-ray microdiffraction. When the electric field exceeds the built-in flexoelectric field, the net interfacial electrical polarization is reconstructed inversely, resulting in a change in the electromechanical response and phase transformation. These results establish flexoelectric coupling at nanoscale interfaces as an alternative, electrically controllable pathway for dynamic phase engineering in complex material systems.

New concepts

Flexoelectric coupling under an applied electric field has largely been discussed in terms of field-induced lattice strain, mainly to separate flexoelectric contributions from conventional piezoelectric responses. In contrast, our study proposes a conceptually different role: flexoelectric polarization–electric field coupling can drive a reversible phase transformation. Starting from the fact that epitaxial relaxation creates a nanoscale interfacial strain gradient layer, our investigation demonstrates that the flexoelectric polarization–electric field coupling can modulate tetragonality of the strain gradient layer, thereby triggering transformation between competing phases. A key implication is that the driving factor is the flexoelectric-field coupling, so the approach is not limited to intrinsically piezoelectric materials and can extend to centrosymmetric dielectrics. This provides a simple design route for nanoscale phase control in complex dielectric architectures (*e.g.*, superlattices) and allows tuning elastic, dielectric, and optical responses without relying on doping or defect/stoichiometry engineering.

1. Introduction

The flexoelectric effect refers to the generation of electric polarization in response to a strain gradient inside materials.[1–8] Since its theoretical prediction in the mid-20th century,[9] the flexoelectric phenomenon has attracted increasing research interest following advances in experimental techniques for probing nanoscale electromechanical coupling.[10–18] Unlike the piezoelectric effect, which exists only in noncentrosymmetric crystals, flexoelectricity is a universal property of all dielectrics.[1,4,6] The flexoelectric effect becomes particularly significant at reduced dimensions, such as in thin films and interfaces, because the extent of the strain gradient increases at smaller scales. Recent studies have shown that external forces can manipulate flexoelectric polarization. Examples include mechanically written polarization domains[8,19–21] and polarization rotation[5,17,22] in ferroelectrics. This finding indicates that the coupling between flexoelectric polarization and external stimuli can change the energy landscape of materials.

Applying an electric field to the flexoelectric polarization provides a direct coupling effect greater than the mechanical force and can induce a substantial change in the thermodynamic energy.[23] To date, most research on the coupling between flexoelectric polarization and an electric field has focused on characterizing lattice deformation in thin ferroelectric oxide films to distinguish between piezoelectric and

---

[a] *Department of Materials Science and Engineering, Gwangju Institute of Science and Technology, Gwangju, South Korea. E-mail: jyjo@gist.ac.kr*
[b] *Pohang Accelerator Laboratory, Pohang University of Science and Technology, Pohang, South Korea*
[c] *Department of Energy Engineering, Korea Institute of Energy Technology, Naju, South Korea*
[d] *Department of Materials Science and Engineering, Kangwon National University, Samcheok, South Korea. E-mail: hjlee.mse@kangwon.ac.kr*
[e] *GIST InnoCORE AI-Nano Convergence Institute for Early Detection of Neurodegenerative Diseases, Gwangju Institute of Science and Technology, Gwangju, South Korea*

flexoelectric responses.[17,24–29] This has led to the development of advanced methods for measuring the flexoelectric coefficient. The research field stands to benefit from broader exploration beyond the measurement of lattice deformation and coefficient extraction. Lattice deformation caused by flexoelectric polarization–electric field coupling can drive phase transformation in polymorphic materials sensitive to lattice changes.[30,31] However, the consequences of this coupling effect on the stability of competing phases have not yet been probed, which has limited the scope of flexoelectric polarization research. In this study, we report the discovery and physical mechanism of the electric field-induced phase transformation from a strain gradient interfacial layer with flexoelectric polarization to the polymorphic crystalline phase in an epitaxial perovskite oxide thin film.

During epitaxial thin film growth, an internal in-plane strain gradient across the film thickness generates a thin interfacial layer that connects the coherently strained and fully relaxed layers.[7,26] This interfacial layer exhibits flexoelectric polarization (P_{flexo}) along the thickness direction because of electromechanical coupling,[32,33] referred to as the flexoelectric layer. The application of an external electric field (E_{ext}) can change the magnitude of P_{flexo}; thus, the lattice of the flexoelectric layer can expand or contract depending on the direction of E_{ext}, as shown in Fig. 1a. For perovskite oxides in which the thermodynamic potential of polymorphic phases is sensitive to tetragonality (defined by the ratio of c/a lattice parameters), the direct coupling between E_{ext} and P_{flexo} can be a route to induce phase transformation.

Here, we focus on how this coupling can serve as a practical and reversible mechanism for driving phase transformation at the nanoscale flexoelectric layer. Using *in situ* X-ray microdiffraction, we reveal how electric fields modulate lattice distortion and induce transitions, providing a direct experimental pathway to control the structural order at the atomic scale. Our findings not only challenge prevailing phenomenological models of field-induced phase transformation in perovskite oxides but also establish flexoelectricity as a powerful tool for dynamic phase engineering in complex material systems.

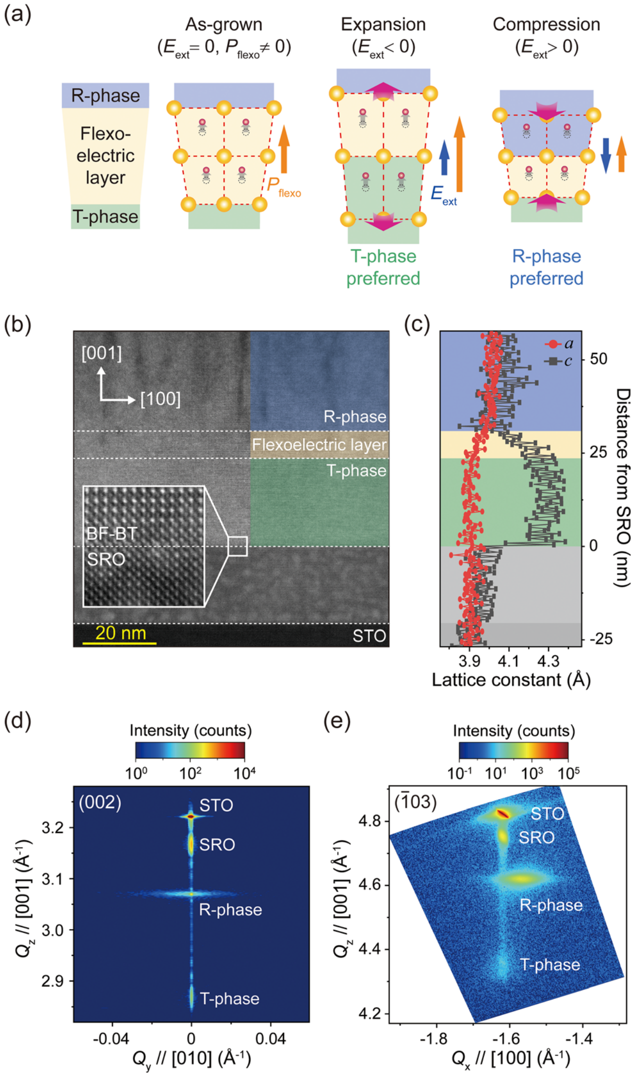

Fig. 1 Structure and hypothesized flexoelectric coupling-driven phase transformation in a BF–BT thin film. (a) Mechanisms of the electric field-induced phase transformation at the flexoelectric layer in an epitaxial BF–BT thin film. (b) High-resolution cross-sectional HAADF STEM image near the $SrTiO_3$ substrate. The inset shows a coherently matched interface between BF–BT (T-phase) and $SrRuO_3$ films. (c) In-plane *a*-axis lattice and out-of-plane *c*-axis lattice parameters of the BF–BT thin film as a function of distance from the $SrRuO_3$ bottom electrode. (d) Symmetric RSM near the (002) reflection and (e) asymmetric RSM near the (−103) reflection for $SrTiO_3$, $SrRuO_3$, R-phase, and T-phase.

2. Experimental section

2.1. Fabrication of the epitaxial $BiFeO_3$–$BaTiO_3$ (BF–BT) thin film

The 215 nm-thick BF–BT thin film was epitaxially grown on a (00*l*)-oriented $SrTiO_3$ (STO) substrate with a 0.5° miscut toward the [100] direction using pulsed laser deposition (PLD) with a KrF excimer laser (λ = 248 nm). The BF–BT thin film was deposited by ablating the ceramic target with a composition of 0.02 at% $(Ba_{0.8}Ca_{0.2})ZrO_3$ (BCZ)-doped 0.67BF–0.33BT with a repetition rate of 2 Hz at a substrate temperature of 630 °C under an oxygen partial pressure of 1 mTorr. After the growth process, the film was slowly cooled to room temperature, gradually in 100 Torr of oxygen. The doped BCZ is to minimize the leakage current of the BF–BT thin film. The 20 nm-thick $SrRuO_3$ (SRO) film is grown on the STO substrate as a bottom electrode layer to form a parallel capacitor structure with a 50 nm-thick Pt top electrode. The Pt top electrode layer with a diameter of 60 μm was deposited on the BF–BT thin film by an e-beam evaporator at room temperature.

2.2. Structural characterization

The crystal structure, morphology, and strain state were investigated using cross-sectional scanning transmission electron microscopy (STEM) and X-ray diffraction (XRD) in this study. High-angle annular dark-field (HAADF) STEM (JEM-ARM300F2 equipped with a Cs-corrector JEOL) was operated at 200 kV with a pixelated detector. The BF–BT specimen for STEM was prepared by focused ion beam milling (Helios G5 UX, Thermo Fisher Scientific). The X-rays with a photon energy of 10 keV were used at the 9C beamline of the Pohang Accelerator Laboratory (PAL). Diffracted X-rays were detected using a gated pixel array detector (Pilatus 100 K, Dectris).

2.3. Time-resolved X-ray microdiffraction (TR-μXRD)

The TR-μXRD technique is utilized to observe electrically driven phase transformation of the BF–BT thin film. The concept of the pump–probe TR-μXRD synchronizes the time of the gate pulse and electric pulse to acquire the scattered intensity in reciprocal space during the application of the E_{ext}. A delay generator (DG 645, Stanford Research System) is used to synchronize the time zero by generating the reference signals to the X-ray detector and function generator (Keysight 81150A-002, Keysight Technology). The X-ray beams were focused on the Pt top electrode with a size of 18.2 μm (horizontal) and 4.1 μm (vertical) using KB mirrors. To avoid any effects arising from charging/discharging time constants of the BF–BT capacitor, the area detector was gated with a duration of 1 μs after 3 μs from the beginning of a 5 μs-width electric pulse, which was completed within 700 ns (Fig. S7). The diffraction patterns for the R- and T-phases are accumulated while applying 20 000 electric pulses at each voltage step to secure adequate diffracted intensity.

2.4. Kinematic diffraction calculation

The diffracted intensity I at wave vector Q in reciprocal space is determined by its structure factor F following, $I(Q) \propto |F(Q)|^2$. The $F(Q)$ is described as $\sum_j f_j \exp(-i\vec{Q}\cdot\vec{r}_j)$, where f_j, $\vec{r}_j$, and $\vec{Q}$ are the atomic form factor and real positions in the unit cell and scattering vector, respectively. The f_j is $f_j^0 + f_j' + if_j''$, where f_j^0, f_j', and if_j'' are the non-resonant atomic form factor, and, real part and imaginary part of the dispersion correction of atom j. For simulations, we calculate the scattering factor and atomic positions using a weighted average, considering the composition of 0.67BF–0.33BT. The scattering factor for each atom at 10 keV is provided at https://henke.lbl.gov/optical_constants/asf.html and summarized in Table S1. The atomic positions based on crystal structures are summarized in Table S2. The c-axis lattice parameters for the flexoelectric layer are considered to be with a linear distribution changing from 4.318 Å to 4.077 Å, which is the measured values from XRD and STEM results, with the number of unit cells.

3. Results and discussion

3.1. Structural characterization of the epitaxial BF–BT thin film

A heteroepitaxial $BiFeO_3$–$BaTiO_3$ (BF–BT) thin film is an excellent model system for investigating phase transformation driven by the coupling between P_{flexo} and E_{ext} owing to the formation of a large P_{flexo} in the flexoelectric layer. Polymorphic phases can coexist across the thickness in the BF–BT thin film grown on $SrTiO_3$ (STO), resulting in a large strain gradient arising from the lattice mismatch between polymorphic phases. The epitaxially grown BF–BT thin film consists of three distinct regimes: (1) a coherently strained layer with an in-plane lattice parameter similar to that of the substrate, (2) a fully relaxed layer with the same crystal phase as bulk BF–BT, and (3) a flexoelectric layer bridging the coherently strained and fully relaxed layers. Below the critical thickness (t_c) where strain relaxation occurs, the compressive misfit strain between BF–BT and the STO substrate produces the tetragonal phase (T-phase) of BF–BT.[34] Above the flexoelectric layer, a rhombohedral phase (R-phase) forms. Owing to the large in-plane lattice mismatch between the R- and T-phases, a large flexoelectricity comparable to the spontaneous polarization of conventional ferroelectrics can be introduced into this flexoelectric layer between the two polymorphic phases.

The application of a negative field parallel to P_{flexo} induces expansion of the c-axis lattice of the flexoelectric layer, resulting in an increase in its tetragonality. This expansion can lead to phase transformation into the T-phase due to its thermodynamic stability, which favors polarization along [001], as predicted by phenomenological thermodynamics models.[35–38] On the other hand, the flexoelectric layer can transform into the R-phase under a positive field antiparallel to P_{flexo} since the compression of the c-axis lattice of the layer results in the lowest energy for the R-phase.

The cross-sectional high-angle annular dark field (HAADF) scanning transmission electron microscopy (STEM) images (Fig. 1b and Fig. S1) reveal three regimes in the 215 nm-thick BF–BT thin film grown on the SRO/STO substrate: a coherently strained T-phase, a fully relaxed R-phase, and a flexoelectric layer. The vertical line contrast observed in the upper BF–BT region is resolved more clearly using the TEM multi-slice electron ptychography image (Fig. S2a). The atomic arrangement across the vertical line in atomic-mapping images (Fig. S2b and c) shows a translational shift of the perovskite sublattice, which is characteristic of an antiphase boundary (APB).[39,40]

We quantify the changes in the in-plane a-lattice and out-of-plane c-lattice parameters along the growth direction in Fig. 1c by analyzing the intensity variations from Fig. 1b. Up to a thickness of 23 nm, the in-plane lattice parameters of the BF–BT thin film match the lattice parameter of the cubic STO substrate (a = 3.905 Å), indicating that the t_c value of the BF–BT epitaxial film on the SRO/STO substrate is 23 nm. Beyond t_c, the in-plane lattice parameter changes gradually over a relaxation length of approximately 6 nm—which is comparable to the flexoelectric layer thickness reported in other strain-graded oxide thin films.[7,22,33] Above this flexoelectric layer, the in-plane lattice parameter becomes uniform and approaches the bulk value of the parent phase (a = 4.032 Å), confirming full relaxation of the compressive strain. The measured in-plane and out-of-plane lattice spacings are 3.90 Å and 4.32 Å, respectively, for the coherently strained T-phase. For the fully relaxed

R-phase, the corresponding values are 4.02 Å and 4.08 Å in pseudocubic notation. The lattice parameters measured *via* TEM match those from the X-ray diffraction (XRD) studies in Fig. 1d and e (see the SI for details). The pseudocubic angle (α_{pc}) of R-phase can be determined by analyzing the symmetry of the asymmetric (-103) reflection, yielding $\alpha_{pc} \approx 89.93^\circ$.

A very large flexoelectric polarization can arise within the flexoelectric layer because of the abrupt tetragonality mismatch between the adjacent R- and T-phases across its interface. The in-plane strain linearly decreases from -3.15 to 0% in the flexoelectric layer within a thickness of 6 nm, which results in an in-plane strain gradient ($\partial u_{yy}/\partial t$) of $\sim 4 \times 10^6$ along the [001] direction (Fig. S3). ∂u_{yy} and $\partial t_{\text{flexo}}$ denote the variations in the in-plane strain and the thickness of the flexoelectric layer, respectively. The P_{flexo} is estimated by eqn (1) as follows:

$$P_{\text{flexo}} = \varepsilon_r \varepsilon_0 E_{\text{flexo}} = \mu \frac{\partial u_{yy}}{\partial t_{\text{flexo}}} = \gamma \chi \frac{e}{a} \frac{\partial u_{yy}}{\partial t_{\text{flexo}}}, \qquad (1)$$

where ε_0 denotes the permittivity of free space, ε_r is the relative permittivity at room temperature, E_{flexo} is the flexoelectric field, μ is the flexoelectric coefficient, γ is the scaling factor, χ is the dielectric susceptibility, e is the electronic charge, and a is the lattice parameter. Here, γ is a dimensionless constant that represents the proportional relationship between μ and χ, serving as a key factor in determining the magnitude of the flexoelectric effect.[11] We assume that the γ value is 0.35, which is generally set between 0.2 and 0.5 for BFO thin films.[41–43] By inserting the experimental $\partial u_{yy}/\partial t$ values into eqn (1), we found that a very large E_{flexo} value of 63 MV m^{-1} and a corresponding P_{flexo} value of 23 μC cm^{-2} are generated across the flexoelectric layer. This value is comparable in magnitude to the spontaneous polarization of conventional ferroelectrics.

3.2. *In situ* observation of the phase transformation at the flexoelectric layer

The phase transformation of the flexoelectric layer can affect the diffraction profiles of BF–BT thin films because the effective volume of the crystalline phases can change. The R- and T-phases are located far apart in reciprocal space due to their distinct lattice parameters. The evolution of the diffraction profiles under an electric field was measured using time-resolved X-ray microdiffraction (TR-μXRD),[35,44–46] as illustrated in Fig. 2a. An electric-field sequence was employed to probe hysteresis in the field-induced phase transformation and the effect of switching the net polarization in the flexoelectric layer. Because the estimated flexoelectric field is 63 MV m^{-1}, the positive field amplitude was set above this value to test whether the phase transformation can be induced by switching the net polarization. The negative field was limited to -70 MV m^{-1} because this amplitude exceeds the coercive field of the ferroelectric T-phase, while higher negative fields lead to nonuniform structural responses that are beyond the scope of this study. As shown in Fig. 2b and c, the applied E_{ext} leads to two apparent changes in the diffraction profiles near the (002) reflections of the R- and T-phases: a shift in intensity maxima due to the electromechanical response and a variation in the scattered intensity. While the T-phase reflection appears significantly suppressed under high positive fields in the contour map (Fig. 2c), it remains discernible in the detailed line profiles. Detailed discussion of the high-field behavior, including potential polar reconfiguration, is provided in Section 3.3.

Within the E_{ext} range of -70 MV m^{-1} to 84 MV m^{-1}, the intensity maximum of the R-phase reflection in Fig. 2d shifts toward lower Q_z values regardless of the field direction, while that of the T-phase reflection in Fig. 2e shifts in different directions depending on the field polarity. As shown in Fig. 2f, the R-phase exhibits a symmetric butterfly-shaped piezoelectric strain–electric field curve, indicating that the piezoelectric expansion accompanies the ferroelectric polarization reversal in the R-phase.[48] In contrast, the T-phase shows an asymmetric strain curve because of the imprinted ferroelectric polarization in the thin layer near the substrate.[39] The weak hysteresis of the piezoelectric response of the R-phase can be attributed to the relaxor-like characteristics of the BF–BT thin film near the morphotropic phase boundary. This relaxor-like behavior is corroborated by the broad temperature-dependent dielectric permittivity (Fig. S4a) and the slim P–E loops with a low coercive field (Fig. S4b), leading to the V-shaped piezoelectric response rather than a conventional butterfly-shaped hysteresis curve. The effective local d_{33} value, determined from the slope of the strain–electric field curve, is ± 34 pm V^{-1} for the R-phase, whereas for the T-phase, it is -57 pm V^{-1} under a negative field and 280 pm V^{-1} under a positive field. The piezoelectric performance of the T-phase is much greater than previously reported values in BiFeO$_3$ and BF–BT thin films ($\sim$48 pm V^{-1}).[34,46,49] The relatively high product of the dielectric permittivity and remnant polarization (εP) in Table S3 suggests an enhanced piezoelectric response, which is consistent with the empirical relation $d_{33} \approx 2Q\varepsilon P$, where Q is the electrostrictive constant.

The lattice distortion of the flexoelectric layer remains unclear in reciprocal space because of the lack of long-range order.

The intensity changes in the R- and T-phase reflections under an electric field provide key insights into the phase transformation from the flexoelectric layer to the R- or T-phases, since the integrated reflection intensity represents the volume fraction of the crystalline phase. As shown in Fig. 2g, the integrated intensity of the T-phase (I_T) increases steadily to -42 MV m^{-1}, reaching a maximum increase of 35%. Above -42 MV m^{-1}, a further increase in the magnitude of negative E_{ext} does not lead to proportional changes in intensity, resulting in a saturated response. In contrast, the integrated intensity of R-phase reflection (I_R) exhibits negligible variation under a negative field.

An opposite trend in intensity changes is observed when a positive field is applied. The I_R increases by 2% when the E_{ext} value increases from 0 to 42 MV m^{-1} and then exhibits a saturated response as the E_{ext} value further increases to 84 MV m^{-1}. The I_T decreases by approximately 50%, which

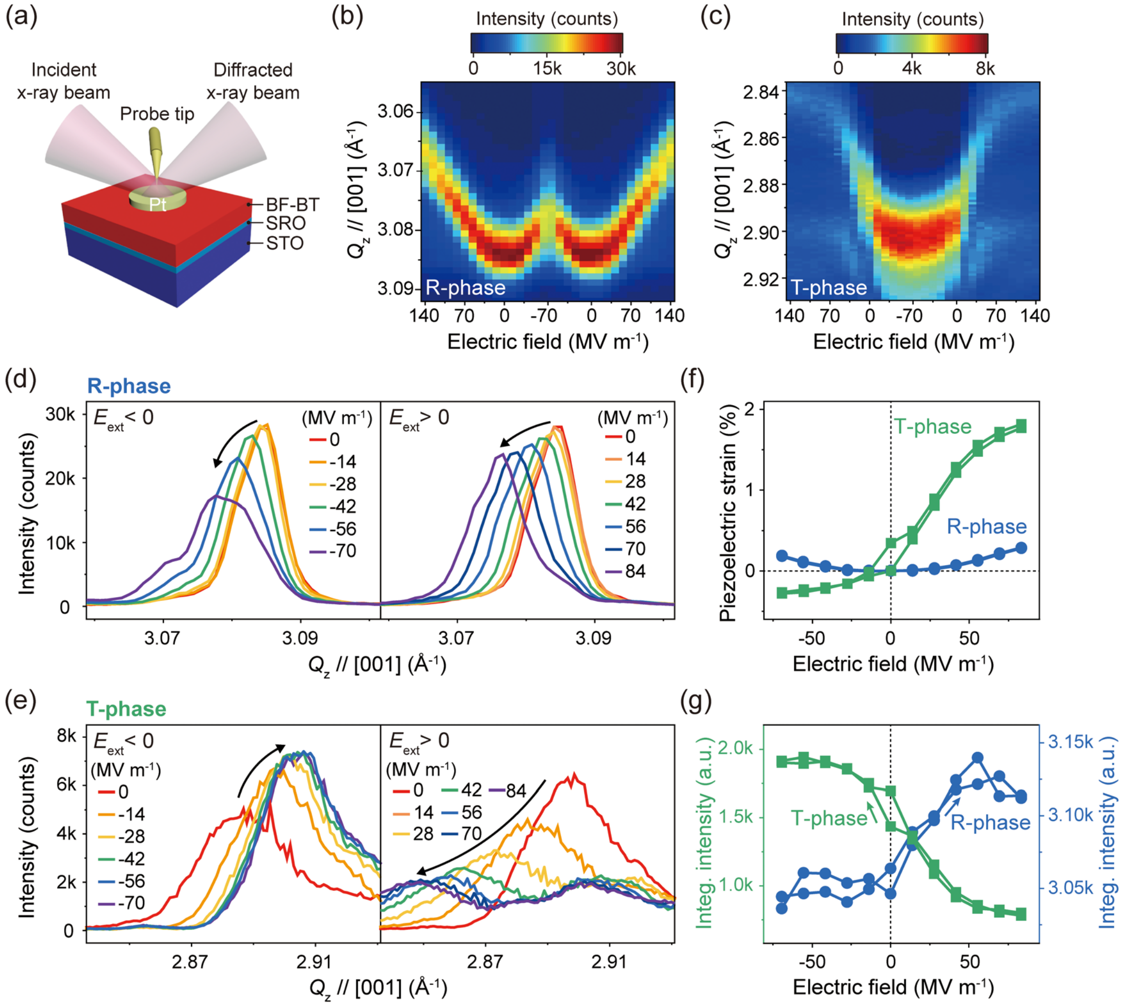

Fig. 2 *In situ* X-ray scattering of the electric-field-induced phase transformation. (a) Schematic of the electric field pump–X-ray scattering probe experiment. (b) and (c) Q_z-electric field contour maps around the (002) Bragg reflection for the R- and T-phases during one cycle of electric field poling under ±140 MV m^{-1}. (d) and (e) XRD profiles of R- and T-phases measured with E_{ext} sequences from 0 to −70 MV m^{-1} and from 0 to 84 MV m^{-1}, respectively. (f) and (g) Electric field dependence of the piezoelectric strain and integrated intensity of the R-phase (blue) and T-phase (green). The unresponsive secondary peak at Q_z = 2.904 Å^{-1}, which can arise from the mechanical clamping imposed by the substrate,[47] was subtracted before integration for the T-phase.

cannot be fully explained by phase transformation alone. This reduction may result from atomic displacement and peak splitting induced by the electric field, making it difficult to separate the effects of structural distortion from those of actual phase transformation. Despite the complexity in analyzing the behavior of the I_T under a positive field, the observed saturation of the intensity of both the R- and T-phases indicates that the transformation can originate from regions with limited volume, such as the flexoelectric layer. The direction of the phase transformation under an electric field is consistent with our intuitive hypothesis regarding the transformation by flexoelectric polarization–field coupling, as described in Fig. 1a.

The change in layer thickness (Δt) can be estimated using the relationship in which the integrated intensity is proportional to the square of the layer thickness. The field-induced Δt can be expressed as $\Delta t = t_{\text{layer}} \times [(I_E/I_0)^{1/2} - 1]$, where t_{layer} is the initial thickness of the crystalline phase layer, and I_0 and I_E are the integrated intensities before E_{ext} and under E_{ext}, respectively. The t_{layer} values for the T- and R-phases are 23 nm and 186 nm, respectively, on the basis of STEM line profile measurements. The calculated maximum Δt is 3.75 nm at E_{ext} = −56 MV m^{-1} for the T-phase and 2.52 nm at E_{ext} = 56 MV m^{-1} for the R-phase. The predicted maximum change in the thickness of the layers is consistent with the thickness limit of the flexoelectric layer. However, estimating the thickness change using only integrated intensities can include uncertainty resulting from several effects, such as polarization changes and crystal orientation.[35,50]

The measurement of the electric field-dependent spacing between Laue oscillations enables the precise determination of thickness changes in the crystalline phase. The intensity distribution of the T-phase reflection in terms of $k = Q_z - Q_{z,(002)}$ is shown in Fig. 3a, emphasizing the change in the spacing between the (002) Bragg reflection and the thickness fringe.

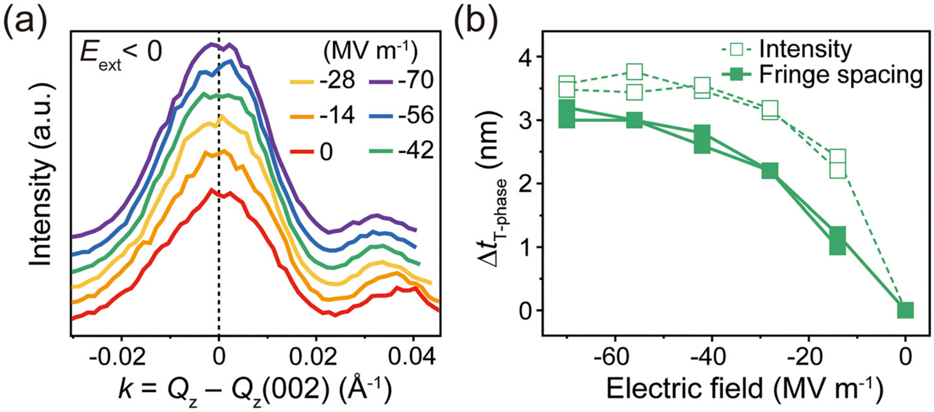

Fig. 3 Electric-field-dependent lattice modulation of the T-phase. (a) Diffraction profiles of the (002) T-phase reflection plotted as $k = Q_z - Q_z(002)$ for the E_{ext} sequence from 0 to −70 MV m^{-1}. (b) Changes in the thickness of the T-phase estimated from the integrated intensity (dashed line) and Bragg–fringe spacing (solid line) as a function of the E_{ext} amplitude.

The decrease in the spacing under a negative field indicates an increase in the thickness of the T-phase, on the basis of the reciprocal relationship between the thickness and the Bragg–Fringe spacing.[51] The direction of changes in the thickness inferred from the spacing changes is opposite to the piezoelectric response of the T-phase, indicating that the effect of piezoelectric distortion on the spacing change can be excluded.

Kinematic diffraction simulations were employed to interpret the measured spacing between the Bragg reflection and the fringe. The field-dependent thickness changes were determined by comparing the experimental data with the simulated profiles, using the root-mean-square difference as a criterion for optimal matching. We assumed that the total film thickness remained constant, considering that the phase transformation was spatially confined to the flexoelectric layer, as depicted in Fig. S5. Detailed information for the diffraction simulation is provided in the SI.

The thickness changes derived from Bragg–fringe spacing are plotted together with the estimation from the integrated intensity changes in Fig. 3b. Both approaches consistently show an increase in T-phase thickness under a negative field. The maximum change in the thickness of the T-phase ($\Delta t_{T\text{-phase}}$ = 3.2 nm) measured from the Bragg peak–fringe spacing is also consistent with the thickness limit of the flexoelectric layer. The observed saturation indicates a transformation confined to the region with limited volume. This agreement demonstrates the reliability of thickness estimation from variations in Bragg–fringe spacing, arising from phase transformation driven by direct coupling between flexoelectric polarization and the electric field.

Notably, our observations deviate from the widely observed field-induced phase transformation in perovskite $BiFeO_3$-based material systems. In highly compressive-strained $BiFeO_3$ films exhibiting coexistence of R- and T-phases along the lateral direction, field-induced lattice expansion has been reported to mediate the R- to T-phase transformation, whereas lattice contraction induces the reverse process.[35,37,45,46,52] In contrast, our diffraction results under the electric field show an opposite trend: the T-phase intensity increases with lattice contraction of the T-phase, whereas the R-phase intensity increases with lattice expansion of the T-phase. This inconsistency suggests that the observed transformation mechanism differs from conventional models based on purely crystalline phases, indicating the need for alternative frameworks that consider the structural complexity of epitaxial thin films.

3.3. Electric field-induced switching of the net electrical polarization of the flexoelectric layer

Further insight into the contributions of P_{flexo}–E_{ext} coupling to the phase transformation can be obtained by applying an electric field that greatly exceeds the internal field in the flexoelectric layer (E_{flexo} = 63 MV m^{-1}). With increasing E_{ext} from 84 MV m^{-1} to 140 MV m^{-1}, the intensity maxima of both the R- and T-phases in Fig. 4a and b shift toward lower Q_z values. These crystalline phases show linear piezoelectric expansion, as shown in Fig. 4c, indicating that they remain stable even under high electric fields. The direction of piezoelectric distortion is consistent with that observed in the low-field regime (below 84 MV m^{-1}), suggesting the absence of ferroelectric polarization reversal in the crystalline layers up to E_{ext} of 140 MV m^{-1}.

The integrated intensity of the R-phase reflection gradually decreases when the applied electric field exceeds 84 MV m^{-1}, in contrast to the monotonic increase and saturation observed in the low-field regime. The integrated intensity of the R-phase decreases by 1.3%, while the T-phase reflection still shows a negligible change (Fig. 4d). The subsequent decrease in the volume of the R-phase is associated with the field-driven switching of the net interfacial polarization. In this high positive field regime, the net electrical polarization of the flexoelectric layer can be reconstructed against the built-in flexoelectric field, thereby changing the direction of the phase transformation. This high-field regime provides direct evidence that the phase fraction is not merely saturated but can be electrically reconfigured once E_{ext} exceeds the effective flexoelectric field.

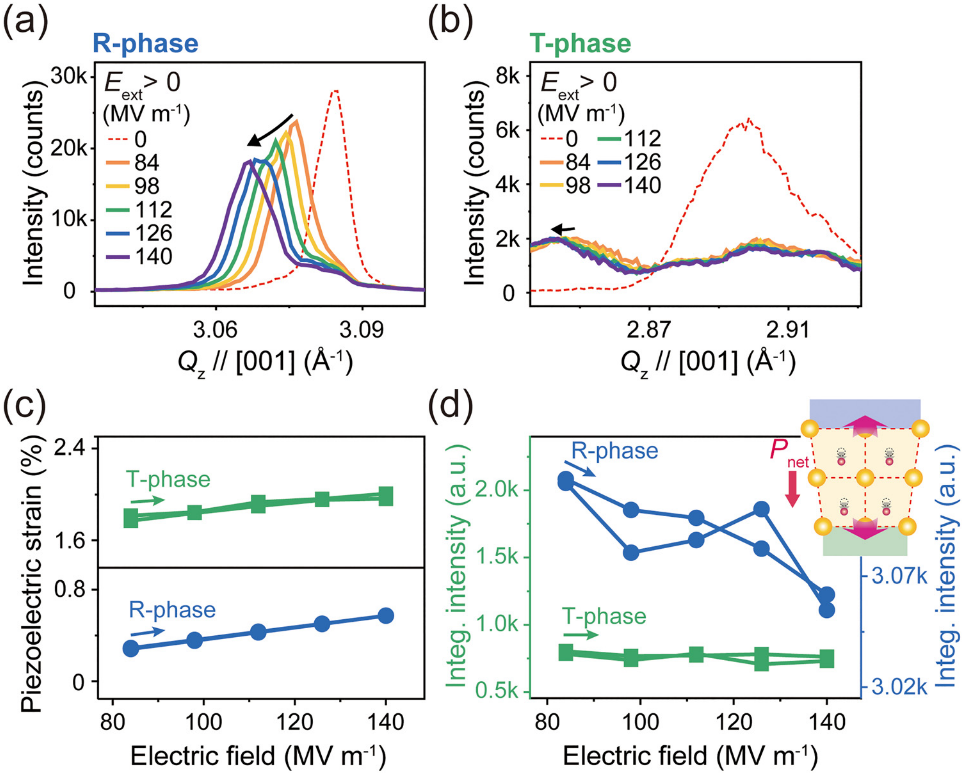

Fig. 4 High-field structural response of R- and T-phases. (a) and (b) XRD profiles of the R- and T-phases measured in the E_{ext} sequence from 84 to 140 MV m^{-1}. (c) Piezoelectric strain and (d) intensity variation of the R- (blue) and T-phases (green) as a function of the applied E_{ext}. The arrow in the scheme of (d) refers to a net electrical polarization.

4. Conclusion

In summary, through an *in situ* TR-μXRD study, we demonstrated that the coupling between P_{flexo} and E_{ext} can emerge as a practical approach to drive phase transformations in the nanoscale flexoelectric layer of epitaxial $BiFeO_3$–$BaTiO_3$ thin films. This transformation is governed by lattice distortion in the flexoelectric layer arising from the electromechanical response of P_{flexo} to E_{ext}. The changes in the phase transformation direction depending on the polarization direction of the flexoelectric layer indicate that this direct coupling is the key factor controlling the phase transformation. By decoupling field-induced phase engineering from the intrinsic piezoelectricity, our findings can apply to a broad class of centrosymmetric dielectrics. This concept further suggests opportunities for controlling nanoscale ordering in complex dielectric systems such as superlattices. Reversible tuning of the phase fraction can result in changes in elastic, dielectric and optical responses without doping or defect/stoichiometry engineering. The results expand the paradigm of flexoelectric electromechanical response toward nanoscale phase control.

Author contributions

Seong Min Park: conceptualization, investigation, methodology, formal analysis, writing – original draft, and writing – review & editing. WooJun Seol: formal analysis and writing – review & writing. Su Yong Lee: formal analysis. Hyunjin Joh: writing – review & writing. Keeyong Lee: formal analysis. Sang Ho Oh: formal analysis. Hyeon Jun Lee: conceptualization, supervision, investigation, writing – original draft, writing – review & editing, and funding acquisition. Ji Young Jo: conceptualization, supervision, writing – original draft, writing – review & editing, and funding acquisition.

Conflicts of interest

There are no conflicts to declare.

Data availability

The data that supports the findings of this study have been included as part of the supplementary information (SI) and are available from the corresponding authors upon reasonable request. Supplementary information is available. See DOI: https://doi.org/10.1039/d6mh00418k.

Acknowledgements

J. Y. J. acknowledges financial support from the GIST Research Project Grant funded by the GIST in 2026; the InnoCORE program of the Ministry of Science and ICT (GIST InnoCORE KH0860); the National Research Foundation of Korea (NRF) grant funded by the Korea government (MSIT) (RS-2026-2548-1875). H. J. L. acknowledges the support from a 2026 Research Grant from the Kangwon National University and a grant from the Regional Innovation System & Education (RISE) program through the Gangwon RISE Center, funded by the Ministry of Education (MOE) and the Gangwon State (G. S.), Republic of Korea (2026-RISE-10-002).

Notes and references

1 P. Zubko, G. Catalan and A. K. Tagantsev, *Annu. Rev. Mater. Res.*, 2013, **43**, 387–421.
2 H. Ji, S. Zhang, K. Liu, T. Wu, S. Li, H. Shen and M. Xu, *Mater. Horiz.*, 2022, **9**, 2976.
3 F. Li, B. Wang, X. Gao, D. Damjanovic, L.-Q. Chen and S. Zhang, *Science*, 2025, **389**, 39.
4 T. D. Nguyen, S. Mao, Y. W. Yeh, P. K. Purohit and M. C. McAlpine, *Adv. Mater.*, 2013, **25**, 946–974.
5 G. Catalan, A. Lubk, A. H. G. Vlooswijk, E. Snoeck, C. Magen, A. Janssens, G. Rispens, G. Rispens, G. Rijnders, D. H. A. Blank and B. Noheda, *Nat. Mater.*, 2011, **10**, 963–967.
6 X. Jia, R. Guo, J. Chen and X. Yan, *Adv. Funct. Mater.*, 2025, **35**, 2412887.
7 D. Lee, A. Yoon, S. Y. Jang, J.-G. Yoon, J.-S. Chung, M. Kim, J. F. Scott and T. W. Noh, *Phys. Rev. Lett.*, 2011, **107**, 057602.
8 J. H. Lee, H. J. Kim, J. Yoon, S. Kim, J. R. Kim, W. Peng, S. Y. Park, T. W. Noh and D. Lee, *Phys. Rev. Lett.*, 2022, **129**, 117601.
9 S. M. Kogan, *Sov. Phys. Solid State*, 1964, **5**, 2069.
10 W. Ma and E. Cross, *Appl. Phys. Lett.*, 2001, **79**, 4420–4422.
11 L. E. Cross, *J. Mater. Sci.*, 2006, **41**, 53–63.
12 P. Zubko, G. Catalan, A. Buckley, P. R. Welche and J. F. Scott, *Phys. Rev. Lett.*, 2007, **99**, 167601.
13 R. Resta, *Phys. Rev. Lett.*, 2010, **105**, 127601.
14 W. Peng, S. Y. Park, C. J. Roh, J. Mun, H. Ju, J. Kim, E. K. Ko, Z. Liang, S. Hahn, J. Zhang, A. M. Sanchez, D. Walker, S. Hindmarsh, L. Si, Y. J. Jo, Y. Jo, T. H. Kim, C. Kim, L. Wang, M. Kim, J. S. Lee, T. W. Noh and D. Lee, *Nat. Phys.*, 2024, **20**, 450–455.
15 K. Chu, B.-K. Jang, J. H. Sung, Y. A. Shin, E.-S. Lee, K. Song, J. H. Lee, C.-S. Woo, S. J. Kim, S.-Y. Choi, T. Y. Koo, Y.-H. Kim, S.-H. Oh, M.-H. Jo and C.-H. Yang, *Nat. Nanotechnol.*, 2015, **10**, 972–979.
16 J. Wang, C. Yang, D. Qi, N. Lu, C. Chen, G. Tian, H. Fang, K. Song, W. Lv and L. Zheng, *Mater. Horiz.*, 2025, **12**, 2187–2196.
17 S. Cai, Y. Lun, D. Ji, P. Lv, L. Han, C. Guo, Y. Zang, S. Gao, Y. Wei, M. Gu, C. Zhang, Z. Gu, X. Wang, C. Addiego, D. Fang, Y. Nie, J. Hong, P. Wang and X. Pan, *Nat. Commun.*, 2022, **13**, 5116.
18 Y. Zhang, Z. Yan, S. Liu and Y. Qin, *Adv. Mater.*, 2025, e01160.
19 H. Lu, C.-W. Bark, D. E. D. L. Ojos, J. Alcala, C. B. Eom, G. Catalan and A. Gruverman, *Science*, 2012, **336**, 59–61.
20 S. M. Park, B. Wang, S. Das, S. C. Chae, J.-S. Chung, J.-G. Yoon, L.-Q. Chen, S. M. Yang and T. W. Noh, *Nat. Nanotechnol.*, 2018, **13**, 366–370.
21 H. Liu, Q. Lai, J. Fu, S. Zhang, Z. Fu and H. Zeng, *Nat. Commun.*, 2024, **15**, 4556.
22 R. Guzman, L. Maurel, E. Langenberg, A. R. Lupini, P. A. Algarabel, J. A. Pardo and C. Magén, *Nano Lett.*, 2016, **16**, 2221–2227.
23 H. Zhou, J. Hong, Y. Zhang, F. Li, Y. Pei and D. Fang, *EPL*, 2012, **99**, 47003.
24 A. Abdollahi, N. Domingo, I. Arias and G. Catalan, *Nat. Commun.*, 2019, **10**, 1266.
25 S. Sharma, R. Kumar, M. Talha and R. Vaish, *Adv. Theory Simul.*, 2021, **4**, 2000158.
26 U. K. Bhaskar, N. Banerjee, A. Abdollahi, Z. Wang, D. G. Schlom, G. Rijnders and G. Catalan, *Nat. Nanotechnol.*, 2016, **11**, 263–266.
27 Q. Liu, S. S. Nanthakumar, B. Li, T. Cheng, F. Bittner, C. Ma, F. Ding, L. Zheng, B. Roth and X. Zhuang, *J. Phys. Chem. C*, 2024, **128**, 16265–16273.
28 J. Y. Fu, W. Zhu, N. Li and L. E. Cross, *J. Appl. Phys.*, 2006, **100**, 024112.
29 L. Shu, Z. Wang, R. Liang, Z. Zhang, S. Shu, C. Tang, F. Li, R.-K. Zheng and S. Ke, *Phys. Rev. B*, 2022, **106**, 024108.
30 R. E. Cohen, *Nature*, 1992, **358**, 136–138.
31 R. D. King-Smith and D. Vanderbilt, *Phys. Rev. B: Condens. Matter Mater. Phys.*, 1994, **49**, 5828–5844.
32 D. Lee, B. C. Jeon, A. Yoon, Y. J. Shin, M. H. Lee, T. K. Song, S. D. Bu, M. Kim, J.-S. Chung, J.-G. Yoon and T. W. Noh, *Adv. Mater.*, 2014, **26**, 5005–5011.
33 M. Wu, Z. Jiang, X. Lou, F. Zhang, D. Song, S. Ning, M. Guo, S. J. Pennycook, J.-Y. Dai and Z. Wen, *Nano Lett.*, 2021, **21**, 2946–2952.
34 Y.-Q. Hu, N.-T. Liu, J. Lao, R.-H. Liang, X. Deng, Z. Guan, B.-B. Chen, H. Peng, N. Zhong, P.-H. Xiang and C.-G. Duan, *ACS Appl. Mater. Interfaces*, 2022, **14**, 36825–36833.
35 M. P. Cosgriff, P. Chen, S. S. Lee, H. J. Lee, L. Kuna, K. C. Pitike, L. Louis, W. D. Parker, H. Tajiri, S. M. Nakhmanson, J. Y. Jo, Z. Chen, L. Chen and P. G. Evans, *Adv. Electron. Mater.*, 2016, **2**, 1500204.
36 Y. D. Liou, S.-Z. Ho, W.-Y. Tzeng, Y.-C. Liu, P.-C. Wu, J. Zheng, R. Huang, C.-G. Duan, C.-Y. Kuo, C.-W. Luo, Y.-C. Chen and J.-C. Yang, *Adv. Mater.*, 2021, **33**, 2007264.
37 D. Edwards, N. Browne, K. M. Holsgrove, A. B. Naden, S. O. Sayedghaee, B. Xu, S. Prosandeev, D. Wang, D. Mazumdar, M. Duchamp, A. Gupta, S. V. Kalinin, M. Arredondo, R. G. P. McQuaid, L. Bellaiche, J. M. Gregg and A. Kumar, *Nanoscale*, 2018, **10**, 17629–17637.
38 R. J. Zeches, M. D. Rossell, J. X. Zhang, A. J. Hatt, Q. He, C.-H. Yang, A. Kumar, C. H. Wang, A. Melville, C. Adamo, G. Sheng, Y.-H. Chu, J. F. Ihlefeld, R. Erni, C. Ederer, V. Gopalan, L. Q. Chen, D. G. Schlom, N. A. Spaldin, L. W. Martin and R. Ramesh, *Science*, 2009, **326**, 977–980.
39 X. Wei, A. K. Tagantsev, A. Kvasov, K. Roleder, C. Jia and N. Setter, *Nat. Commun.*, 2014, **5**, 3031.

40 Y. Zhang, M. Han, D. Sando, L. Wu, N. Valanoor and Y. Zhu, *ACS Appl. Electron. Mater.*, 2021, **3**, 3226–3233.

41 B. C. Jeon, D. Lee, M. H. Lee, S. M. Yang, S. C. Chae, T. K. Song, S. D. Bu, J.-S. Chung, J.-G. Yoon and T. W. Noh, *Adv. Mater.*, 2013, **25**, 5643–5649.

42 D. Lee, S. M. Yang, J. G. Yoon and T. W. Noh, *Nano Lett.*, 2012, **12**, 6436–6440.

43 R. Guo, L. You, W. Lin, A. Abdelsamie, X. Shu, G. Zhou, S. Chen, L. Liu, X. Yan, J. Wang and J. Chen, *Nat. Commun.*, 2020, **11**, 2571.

44 H. J. Lee, T. Shimizu, H. Funakubo, Y. Imai, O. Sakata, S. H. Hwang, T. Y. Kim, C. Yoon, C. Dai, L. Q. Chen, S. Y. Lee and J. Y. Jo, *Phys. Rev. Lett.*, 2019, **123**, 217601.

45 Y. Ahn, A. Pateras, S. D. Marks, H. Xu, T. Zhou, Z. Luo, Z. Chen, L. Chen, X. Zhang, A. D. DiChiara, H. Wen and P. G. Evans, *Phys. Rev. Lett.*, 2019, **123**, 045703.

46 H. J. Lee, J. Kim, S. H. Hwang, H. Choe, S. Gorfman, Y.-J. Heo, S. Y. Lee, P.-E. Janolin, I. Kornev, T. U. Schülli, C. Richter, J.-H. Lee, U. Pietsch, C.-H. Yang and J. Y. Jo, *APL Mater.*, 2020, **8**, 101110.

47 H. J. Lee, S. S. Lee, J. H. Kwak, Y.-M. Kim, H. Y. Jeong, A. Y. Borisevich, S. Y. Lee, D. Y. Noh, O. Kwon, Y. Kim and J. Y. Jo, *Sci. Rep.*, 2016, **6**, 38724.

48 J. Wu, H. Zhang, C.-H. Huang, C.-W. Tseng, N. Meng, V. Koval, Y.-C. Chou, Z. Zhang and H. Yan, *Nano Energy*, 2020, **76**, 105037.

49 Y. Zhang, F. Xue, Z. Chen, J.-M. Liu and L.-Q. Chen, *Acta Mater.*, 2020, **183**, 110–117.

50 H. J. Lee, E.-J. Guo, T. Min, S. H. Hwang, S. Y. Lee, K. Dörr, J. Lee and J. Y. Jo, *Nano Res.*, 2018, **11**, 3824–3832.

51 A. M. Miller, M. Lemon, M. A. Choffel, S. R. Rich, F. Harvel and D. C. Johnson, *Z. Naturforsch.*, 2022, **77**, 313–322.

52 J. X. Zhang, B. Xiang, O. He, J. Seidel, R. J. Zeches, P. Yu, S. Y. Yang, C. H. Wang, Y.-H. Chu, L. W. Martin, A. M. Minor and R. Ramesh, *Nat. Nanotechnol.*, 2011, **6**, 98–102.